Title

Crystallinity and adhesiveness improvements of Ag thin films by Bi-and Sb-assisted growth

Author(s)

Nishimoto, N., Fujihara, J.

Journal

Applied Physics A, 131(1), 1-11.

Published

2025

URL（The Version of Record）

https://doi.org/10.1007/s00339-024-08156-5

Crystallinity and adhesiveness improvements of Ag thin films by Bi- and Sb-assisted growth

Naoki Nishimoto[1,*], Junko Fujihara[2]

[1] Shimane Institute for Industrial Technology, 1 Hokuryo, Matsue, Shimane 690-0816, Japan

ORCID: 0000-0002-5854-7848

[2] Department of Legal Medicine, Shimane University Faculty of Medicine, 89-1 Enya, Izumo, Shimane 693-8501, Japan

ORCID: 0000-0001-5359-5181

[*] **Corresponding author:**

Naoki Nishimoto

E-mail: nishimoto.su2010@gmail.com

Abstract

Ag thin films are used in a variety of electrical devices, but they easily condense owing to the low cohesive energy of Ag. In this study, Bi- and Sb-assisted growth techniques were utilized to improve the stability of Ag thin films. Thin films of Ag, Bi-doped Ag, and Sb-doped Ag were deposited on polyimide (PI) films at 160 and 320 °C by radio frequency magnetron sputtering. The thin-film orientation and strain were determined by analyzing the X-ray diffraction patterns. In addition, the adhesiveness between the thin films and PI substrates was evaluated by immersion tests. The [111] growth of the Ag thin films was assisted by Bi at 160 °C and by Sb at 320 °C, where the (111) orientation possesses the lowest surface energy for the face-centered cubic structure of the Ag thin films. The strain present in the PI film was not applied to the grown thin films. Doping with Bi or Sb decreased the thin-film strain and prevented the detachment of the Ag thin film from the PI film in pH 9 buffer, with the exception of the Sb-doped Ag thin film grown at 160 °C, which exhibited non-uniform growth. Thus, Bi or Sb doping can suppress the condensation of Ag thin films by enhancing their (111) orientation and adhesiveness to the substrate. The obtained results indicate that Bi- and Sb-assisted growth techniques can stabilize Ag thin films and improve the reliability of devices based on these films.

Keywords:

Sputtering; Ag thin film; Metal-assisted growth; Stacking fault; Thin-film strain; Adhesiveness

Statements and Declarations

Competing interests

The authors declare that they have no conflict of interest.

1. Introduction

Ag is a noble metal with an estimated crustal abundance of 0.08 ppm [1]. Its crystal structure is face-centered cubic (fcc) and its atomic number, atomic weight, and density are 47, 107.9, and 10.49 g cm^{-3}, respectively [2, 3]. Ag is used in a wide variety of applications, such as for the surface treatment of tableware and as a component of dental alloys, because it is a comparatively stable metal with high antibacterial activity [4, 5]. Furthermore, Ag has high thermal conductivity (429 W m^{-1} K^{-1}) and low electrical resistivity (1.59×10^{-6} Ω cm) [6]. These advantageous characteristics have enabled the use of Ag thin films in various electrical devices as reflective and conductive films [7, 8]. However, Ag thin films easily condense owing to their low stability (cohesive energy: 284 kJ mol^{-1}), whereupon they lose their desirable properties [9]. Therefore, it is necessary to enhance the stability of Ag thin films to ensure high device reliability.

Ag thin films can be stabilized by accelerating [111] growth because (111) has the lowest surface energy in the fcc structure [10]. Thin films with the fcc structure readily form a (111)-oriented structure [11–13]. However, structural disorder in thin films, which is caused by insufficient driving force for crystal growth, prevents [111] growth [14, 15]. Metal-assisted growth techniques can compensate for this inadequate driving force. Although various metals have been proposed as potential catalysts for metal-assisted growth [14–19], Bi and Sb are considered the most effective for stabilizing Ag thin films. In our previous studies, Bi suppressed the occurrence of structural disorder in InSb and GaSb thin films, which have a zinc blende structure belonging to the fcc Bravais lattice, and improved their (111) orientation [14, 15]. Ajay et al. reported that a flat (111)B-terminated facet was observed at the growth front of GaAs nanowires containing small amounts of Sb as a surfactant [19]; GaAs also has a zinc blende structure as in the case of InSb and GaSb.

In addition to minimizing the surface energy, improving the adhesiveness between Ag thin films and their substrate is also effective for suppressing condensation. The adhesiveness is affected by the strain present in the Ag thin film. For example, Huang et al. reported that the adhesion energy decreased with increasing tensile strain of the thin film [20]. Moreover, Moridi et al. quantitatively confirmed that the overall film strain was dependent on the dislocation density [21]. Our previous studies indicated that the use of metal-assisted growth decreased the defect density [14, 15], which we speculated may prove useful for improving the adhesiveness between Ag thin films and their substrate.

To our knowledge, there have been no reports on the effect of metal-assisted growth on Ag thin film and the change in adhesiveness with the substrate. The aim of this study was to enhance the stability of Ag thin films by using Bi and Sb doping to both favor the (111) orientation of Ag and improve the adhesiveness of the Ag thin film to a polyimide (PI) film substrate. Thin films of Ag, Bi-doped Ag, and Sb-doped Ag were deposited on PI films by radio frequency (RF) magnetron sputtering. The (111) orientation of the Ag thin films was identified from X-ray diffraction (XRD) patterns. The thin-film strain, which influences the adhesiveness between the grown thin film and the PI film, was analyzed by estimating the strain originating from the PI film and the stacking faults. In addition, the adhesiveness was confirmed experimentally by performing immersion tests.

2. Materials and methods

2.1 Growth of Ag, Bi-doped Ag, and Sb-doped Ag thin films

An RF magnetron sputtering system (HSR-351L, Shimadzu Industrial Systems) was utilized to deposit Ag, Bi-doped Ag, and Sb-doped Ag thin films on PI films (Kapton, DuPont Toray). The PI film surface was first cleaned by reverse sputtering (30 W RF power, Ar atmosphere, room temperature, 10 min). The base pressure of the growth chamber was less than 3.6×10^{-4} Pa. Sputtering was then performed at an RF power of 80 W and a pressure of 0.5 Pa for 15 min under a flow of Ar gas (6N purity), using Ag (4N purity), $Ag_{0.97}Bi_{0.03}$ (3N purity), and $Ag_{0.97}Sb_{0.03}$ (3N purity) targets of two-inch diameter. The Bi and Sb contents in the Ag targets were determined by referring to our previous studies [14, 15]. The substrate temperature was set to 320 °C, which is below the heat-resistant temperature of PI film (400 °C), and was also set to 160 °C (half of 320 °C) to evaluate the temperature dependence of the dopant behavior.

2.2 Thin-film characterization

The Bi and Sb contents of the Ag thin films were measured by X-ray fluorescence (XRF; ZSX Primus IV, Rigaku). The film thickness was estimated using the fundamental parameter method based on the XRF intensity. The crystal structure, structural defects, and thin-film strain were examined by XRD measurements (SmartLab XE, Rigaku) using $CuK\alpha_1$ radiation. This XRD system is equipped with a multilayer mirror in the incident beam line. The surface morphology was visualized by dynamic-mode atomic force microscopy (AFM; NaioAFM, Nanosurf AG). The AFM system was placed on an anti-vibration table (Isostage, Nanosurf AG). Nanosurf Naio software (version 3.10.0.36) was used to analyze the root mean square roughness (Sq).

2.3 Immersion tests

As a preliminary test, samples of the undoped Ag thin film grown on PI film at 160 °C were immersed in 1.5 mL of either 0.1 M sodium acetate buffer (pH 5) or 0.1 M tris buffer (pH 9). To examine the influence of Bi and Sb doping on the adhesiveness, the Ag, Bi-doped Ag, and Sb-doped Ag thin films grown at 160 and 320 °C were immersed in 0.1 M tris buffer (pH 9). Aliquots (0.5 mL) of each solution were removed at various time points (days 3, 7, 14, 21, 28, and 35) and diluted with 1N HNO_3 (4.5 mL). After sampling, the solution was replenished with the corresponding buffer (0.5 mL).

The Ag concentrations in the samples were determined by microwave plasma atomic emission spectrometry (MP-AES; Agilent 4200 MP-AES, Agilent Technologies) using a detection wavelength of 328.068 nm.

Hydride generation (HG) is a useful technique for quantifying hydride-forming elements such as metalloids, with the advantages of efficient matrix removal, low sample loss, and good sensitivity [22, 23]. Sb concentrations in the samples were assayed by HG-MP-AES using the multimode sample introduction system (MSIS) according to our previous method [24]. Sb was detected as antimony hydride (stibine,

SbH_3) using a detection wavelength of 231.147 nm.

Because Bi is a metalloid like Sb, the total Bi levels in the samples were also determined by HG-MP-AES, although it was necessary to develop a different analytical method. Therefore, Bi was analyzed after pretreatment with HCl and $NaBH_4$/NaOH solution at higher concentrations than those used for Sb. The Bi species in the standards and immersion test samples (2.5 mL) were reduced with 20% KI (0.5 mL) followed by acidification with 1.2 N HCl (1 mL). The reduced samples and the $NaBH_4$/NaOH solution (4% w/v; 0.4% w/v, respectively) were introduced into the MSIS. Bi was detected as gaseous bismuth hydride (bismuthine, BiH_3) at a detection wavelength of 223.061 nm.

3. Results and discussion

3.1 Behavior of doped Bi and Sb during Ag thin-film growth

The Bi and Sb contents in the Bi- and Sb-doped Ag thin films were low compared with the nominal compositions of the targets ($Ag_{0.97}Bi_{0.03}$ and $Ag_{0.97}Sb_{0.03}$). According to XRF analysis, the Bi contents in the Bi-doped Ag thin films grown at 160 and 320 °C were 1.13 and 0.45 at%, respectively. In the case of the Sb-doped Ag thin films, Sb was not detected at either growth temperature.

During the thin-film growth process, Bi and Sb segregate to the growth front [25, 26], and the thin-film surface under the sputtering growth can be damaged by the high energy of the source materials [27]. Accordingly, the surface-segregated Bi and Sb are considered to be removed from the thin-film surface by the supplied source materials. Because the diffusion coefficient increases with increasing growth temperature, the lower Bi content at 320 °C was ascribed to the accelerated surface segregation of Bi at the higher growth temperature. Given that the diffusion coefficient of Sb is larger than that of Bi [28], we infer that more Sb became segregated to the thin-film surface compared with Bi and was thus removed from the thin film.

3.2 Influence of Bi and Sb doping on growth mechanism of Ag thin films

Table 1 lists the thicknesses of the Ag, Bi-doped Ag, and Sb-doped Ag thin films grown at 160 and 320 °C. The film thicknesses were calculated based on the deposition amount estimated from the XRF intensity and the density of Ag. The density changes in Ag upon Bi and Sb doping were assumed to be negligible on account of the low Bi and Sb contents in the doped thin films. The film thickness increased with increasing growth temperature and slightly changed upon Bi and Sb doping; the thickness of the Ag thin film (369 nm) at 160 °C decreased to 349 nm with Bi doping and remained almost unchanged (368 nm) with Sb doping, while the thickness of Ag thin film (380 nm) at 320 °C decreased to 363 nm with Bi doping and increased to 394 nm with Sb doping.

Figure 1 presents AFM images showing the surface morphologies of the prepared thin films. For the undoped Ag thin films, increasing the growth temperature led to an increase in the grain size and a decrease in the surface flatness (Fig. 1a, d). A

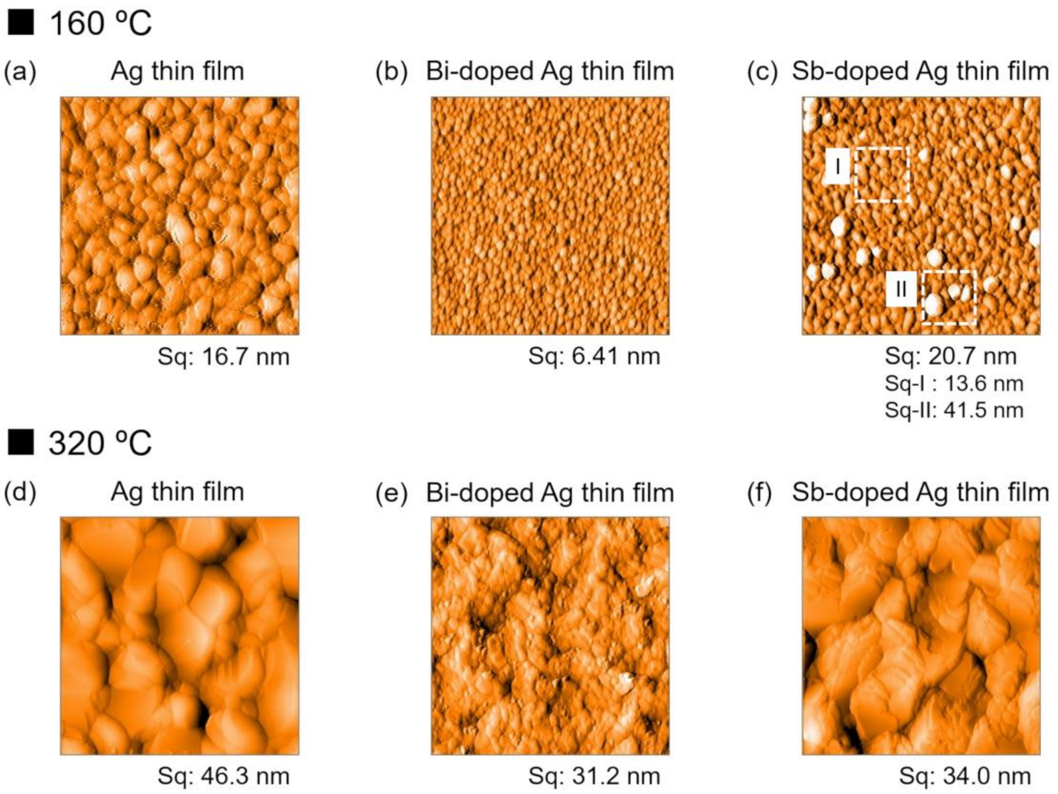

Fig. 1. AFM images of thin films of (a, d) Ag, (b, e) Bi-doped Ag, and (c, f) Sb-doped Ag grown at (a–c) 160 °C and (d–f) 320 °C. The size of each image is 5.0 µm × 5.0 µm, and Sq is the root mean square roughness. Sq-I and -II are Sq of regions I and II in (c), respectively.

smaller grain size and greater surface flatness were also observed in the Bi-doped Ag thin films (Fig. 1b, e) compared with the undoped films (Fig. 1a, d). The decreases in film thickness (Table 1) and grain size upon Bi doping indicate that Bi suppressed the three-dimensional growth of the Ag thin film [26]. By contrast, the effect of Sb doping led to non-uniform growth at 160 °C (Fig. 1c) and appeared uniformly in plane as the formation of crystal facets at 320 °C (Fig. 1f). An increase in the film thickness (Table 1) and a change in the growth mechanism were observed at 320 °C for the Sb-doped Ag thin films. These changes suggest that the two-dimensional growth of the Ag thin films was strengthened at 320 °C upon Sb doping [29].

3.3 Change in the orientation of Ag thin films upon Bi and Sb doping

Figure 2 shows the XRD patterns of the Ag, Bi-doped Ag, and Sb-doped Ag thin films grown at 160 °C (Fig. 2a) and 320 °C (Fig. 2b). To evaluate the (111) orientation of the prepared thin films, Fig. 2c shows a bar graph of $I_{111}/(I_{200}+I_{220})$, where I_{111}, I_{200}, and I_{220} denote the diffraction intensities of the (111), (200), and (220) peaks, respectively. At the growth temperature of 160 °C, a highly (111)-oriented Ag thin film was obtained upon Bi doping, where the I_{200} value of the Bi-doped Ag

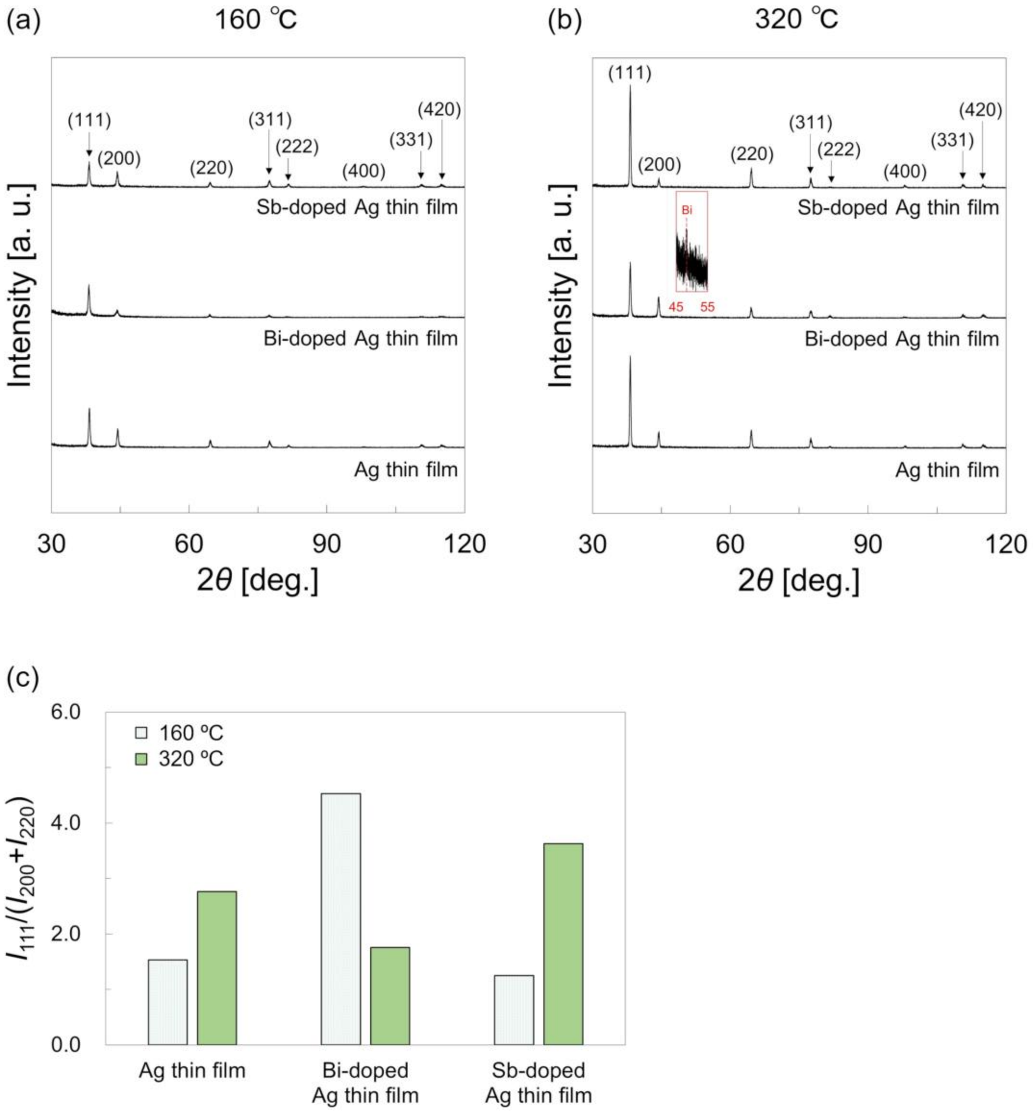

Fig. 2. XRD patterns of Ag, Bi-doped Ag, and Sb-doped Ag thin films grown at (a) 160 °C and (b) 320 °C. (c) Comparison of the $I_{111}/(I_{200}+I_{220})$ intensity ratios of the grown thin films. I_{111}, I_{200}, and I_{220} denote the diffraction intensities of the (111), (200), and (220) peaks, respectively.

thin film was lower than that of the undoped film (Fig. 2a). This was ascribed to suppression of the structural disorder in the Ag thin film upon Bi doping [14, 15]. By contrast, Sb doping led to deterioration of the (111) orientation, where the I_{111} value of the Sb-doped Ag thin film was lower than that of the undoped film at the growth temperature of 160 °C (Fig. 2a). This was attributed to the non-uniform growth of the Sb-doped Ag thin film as mentioned in Section 3.2 (Fig. 1c). On the other hand, the diffraction intensity increased at the growth temperature of 320 °C (Fig. 2b) owing to the faster crystal growth. In particular, the I_{111} values of the thin films greatly increased in all cases because of the high growth rate of the preferred (111) orientation. However, the $I_{111}/(I_{200}+I_{220})$ value for the Bi-doped Ag thin film decreased at the growth temperature of 320 °C. An extremely weak diffraction peak corresponding to Bi-Bi bonds (Bi clusters) was also observed in the XRD pattern of the Bi-doped Ag thin film grown at 320 °C (inset in Fig. 2b). Previously, we reported that the formation of Bi clusters increases structural disorder in the growth of GaSbBi thin film [15]. Thus, the formation of Bi clusters may have increased the structural disorder of the Ag thin film and suppressed [111] growth. By contrast, the (111) orientation was enhanced at 320 °C for the Sb-doped Ag thin film, with a higher I_{111} value and a lower I_{200} value. Hence, the facet shown in Fig. 1f is (111). This result is in agreement with the effect of Sb surfactant during the growth of GaAs nanowires reported by Ajay et al. [19].

3.4 Improved adhesiveness between Ag thin films and PI films upon Bi and Sb doping

3.4.1 Estimation of thin-film strain originating from the PI film

Thin-film strain affects the adhesiveness between a thin film and its substrate, and the effect of differences in the thermal expansion coefficients of the thin film and substrate on the thin-film strain in particular cannot be ignored. Therefore, the thin-film strain originating from the PI films was estimated.

For a defect- and strain-free polycrystalline material, a plot of the lattice parameter a_{hkl} against the diffractometer function $f(\theta) = \cos\theta^2/\sin\theta$ is linear, as given by the following equation [30]:

$$a_{hkl} = a_0 + mf(\theta_{hkl}), \qquad (1)$$

where a_0 is the lattice constant (4.0862 Å for Ag) and m is a constant. Figure 3 shows plots of a_{hkl}, which was obtained from the XRD patterns of the thin films (closed circles), and the solid lines represent Eq. 1. The values of m were determined by fitting the plots of a_{hkl} using the least-squares method. The deviation of a_{hkl} from the linear relation was described as the square sum of the difference between the plotted a_{hkl} and the solid line, $\sum e^2$. By considering defects and strain in Eq. 1, the deviation can be expressed as follows [30]:

$$a_{hkl} = a_0 + mf(\theta_{hkl}) + \left(a_0 G_{hkl} + a_0 \varepsilon_f J_{hkl}\right)SFP + a_0 \sigma S_{hkl}, \qquad (2)$$

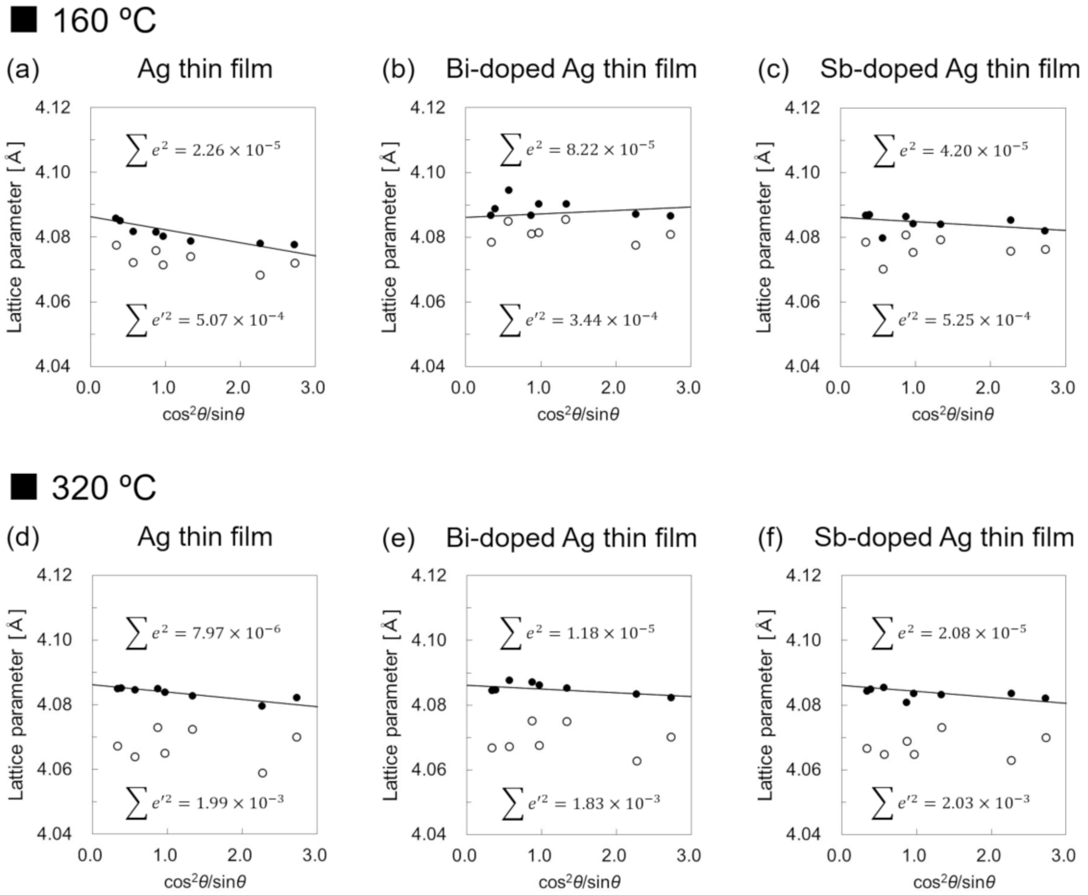

Fig. 3. Plots of the lattice parameter a_{hkl} as a function of $\cos\theta^2/\sin\theta$ for thin films of (a, d) Ag, (b, e) Bi-doped Ag, and (c, f) Sb-doped Ag grown at (a–c) 160 °C and (d–f) 320 °C. The closed circles represent a_{hkl} and the open circles represent a_{hkl} without the strain vertical to the substrate, $a_{hkl} - a_0\varepsilon_{hkl}^{\mathrm{zz}}$. $\sum e^2$ corresponds to the deviation of a plot of a_{hkl} from linearity and $\sum e'^2$ corresponds to the deviation of a plot of $a_{hkl} - a_0\varepsilon_{hkl}^{\mathrm{zz}}$ from linearity.

where G_{hkl} and J_{hkl} are constants that depend on the plane directions, ε_f is the fractional change in interplanar spacing at the fault plane, $SFP\ (= SFP' - SFP'')$ is the stacking-fault probability (SFP' and SFP'' denote the intrinsic and extrinsic stacking-fault probabilities, respectively), and σS_{hkl} $(= \varepsilon_{hkl}^{\mathrm{zz}})$ is the strain vertical to the substrate, which originates from the difference in thermal expansion coefficients between the thin film and substrate (σ and S_{hkl} are the residual strain and elastic constant based on the Reuss assumption and Voigt assumption, respectively). Hence, in the case that $\varepsilon_{hkl}^{\mathrm{zz}}$ is applied to a thin film, the deviation of a plot of $a_{hkl} - a_0 \varepsilon_{hkl}^{\mathrm{zz}}$ from the linear relation, $\sum e'^2$, should become smaller than $\sum e^2$. For a thin film grown on PI film, ε_{hkl}^{zz} is given by the following equation [14]:

$$\varepsilon_{hkl}^{\mathrm{zz}} = \varepsilon^{\parallel} - \varepsilon^{\parallel} \Delta\tilde{\varepsilon}, \qquad (3)$$

where $\Delta\tilde{\varepsilon}$ is the reduced tetragonal distortion calculated for any direction [31] and $\varepsilon^{\parallel}$ is the in-plane thermal strain. $\varepsilon^{\parallel}$ can be estimated using the thermal expansion coefficient of Ag, $\alpha_{\mathrm{Ag}}^{\mathrm{th}}$ (18.9 ppm °C^{-1} [32]), and that of PI, $\alpha_{\mathrm{PI}}^{\mathrm{th}}$ (30 ppm °C^{-1} [33]), as follows [14]:

$$\varepsilon^{\parallel} = \varepsilon^{\mathrm{xx}} = \varepsilon^{\mathrm{yy}} = \left(\alpha_{\mathrm{Ag}}^{\mathrm{th}} - \alpha_{\mathrm{PI}}^{\mathrm{th}}\right)\Delta T, \qquad (4)$$

where ΔT denotes the difference between room temperature (20 °C) and the growth temperature. The open circles in Fig. 3 represent the plotted values of $a_{hkl} - a_0 \varepsilon_{hkl}^{\mathrm{zz}}$ against $\cos\theta^2/\sin\theta$. For all of the thin films, $\sum e'^2$ was larger than $\sum e^2$ (Fig. 3a–f). This result demonstrates that the strain present in the PI film was not applied to the grown thin films.

3.4.2 Stacking-fault probability of the thin films

As mentioned above, the difference in thermal expansion coefficients between the thin films and PI film had little effect on the thin-film strain. Therefore, the changes in the crystallinity of the Ag thin films upon Bi and Sb doping could be assessed from the positions of the diffraction peaks in the XRD patterns (Fig. 2). Stacking faults were considered as the primary defects in the prepared thin films. In austenitic steel with the same fcc structure as Ag, the SFP has been calculated from neighboring diffraction peaks corresponding to (111) and (200) as follows [34–36]:

$$\begin{aligned}(2\theta_{200} - 2\theta_{111})_{\mathrm{CW}} - (2\theta_{200} - 2\theta_{111})_{\mathrm{ANN}} \\ = \frac{-45\sqrt{3}}{\pi^2}\left[\tan\theta_{200,\mathrm{ANN}} + \frac{1}{2}\tan\theta_{111,\mathrm{ANN}}\right] SFP, \qquad (5)\end{aligned}$$

where CW and ANN denote a cold-worked sample and an annealed sample, respectively; the cold-worked sample represents a deformed sample containing residual strain and stacking faults, whereas the annealed sample is free from strain and defects. In the current analysis, θ_{200} and θ_{111} for the CW sample were experimental values obtained from the XRD patterns of each thin film and those for the ANN sample were calculated using a_0 of Ag (4.0862 Å).

Figure 4 shows the changes in SFP upon Bi and Sb doping. Because SFP is defined as $SFP' - SFP''$, SFP' is greater than SFP'' at $SFP > 0$ and SFP' is less than SFP'' at $SFP < 0$. The compressive and tensile strains are increased by increasing SFP' and SFP'', respectively [37]. The SFP values were negative for the undoped Ag thin films, whereas they became positive upon Bi and Sb doping; these changes indicate that the strain in the Ag thin films changed from tensile strain to compressive strain. At the growth temperature of 160 °C (Fig. 4a), the absolute value of SFP, $|SFP|$, decreased upon Bi doping and increased upon Sb doping. This increase in $|SFP|$ upon Sb doping was ascribed to the increase in structural disorder due to non-uniform growth (Fig. 1c). As shown in Fig. 4b, the SFP'' of the undoped Ag thin film increased at the growth temperature of 320 °C compared with that at 160 °C. However, the value of $|SFP|$ significantly decreased upon Bi and Sb doping. Therefore, the

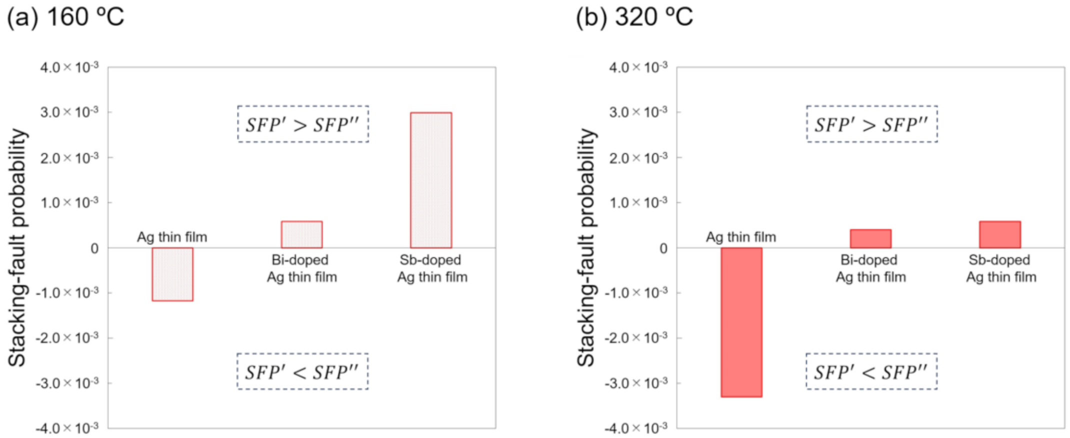

Fig. 4. Estimated stacking-fault probability, SFP, for Ag, Bi-doped Ag, and Sb-doped Ag thin films grown at (a) 160 °C and (b) 320 °C.

doping of Ag thin films with Bi or Sb led to a decrease in the thin-film strain generated by defects, except in the case of the Sb-doped Ag thin film grown at 160 °C.

3.4.3 Immersion tests of the thin films

The adhesiveness between the grown thin films and PI films was evaluated by immersion tests. First, samples of the undoped Ag thin film grown at 160 °C were immersed in pH 5 buffer and pH 9 buffer for 35 days. The results are plotted in Figure 5. For the sample immersed in the pH 9 buffer, Ag eluted from the thin film over the course of the experiment and the thin film had detached from the PI film by day 35. By contrast, the Ag thin film was stable in the pH 5 buffer and little Ag was eluted: Ag has a low ionization tendency and is poorly soluble in weak acid. Hence, immersion tests

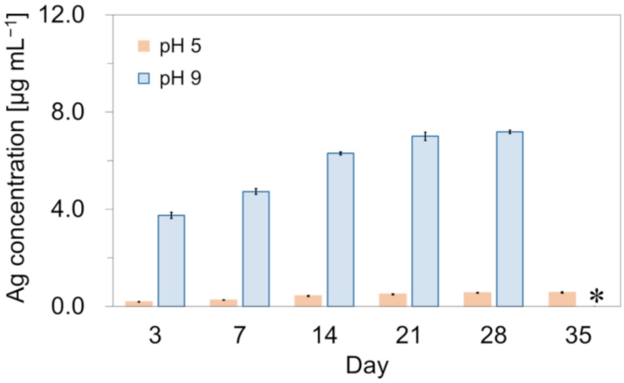

Fig. 5. Ag concentrations eluted in pH 5 and pH 9 buffers from undoped Ag thin films grown at 160 °C. The asterisks (*) indicate that the Ag thin film had detached from the PI film. Data are expressed as the average ± standard deviation.

were performed in pH 9 buffer to evaluate any changes in adhesiveness due to Bi and Sb doping.

Figure 6 shows the eluted Ag, Bi, and Sb concentrations from the thin films over 35 days of immersion in pH 9 buffer. Although the Ag concentrations eluted from the undoped thin film grown at 320 °C were lower than those from the undoped thin film grown at 160 °C, the former had detached from the PI film by day 21, whereas the latter only became detached by day 35 (Fig. 6a). By contrast, the Bi-doped Ag thin films did not detach from the PI film at all and the eluted Ag concentrations remained approximately constant over the course of the experiment (Fig. 6b). Compared with the undoped thin film (Fig. 6a), Ag elution was accelerated at 160 °C and suppressed at 320 °C (Fig. 6b). Meanwhile, the eluted Bi concentrations decreased over the course of the experiment until 21 days, after which Bi was not detected, and the eluted Bi concentrations were higher at the growth temperature of 160 °C than at 320 °C (Fig. 6c). By contrast, the Sb-doped Ag thin film grown at 160 °C detached from the PI film on day 9, whereas that grown at 320 °C did not detach until day 28 (Fig. 6d). However, the Ag concentrations eluted from the Sb-doped Ag thin film (Fig. 6d) were slightly lower than those from the undoped film (Fig. 6a). Highly toxic Sb was not detected at either growth temperature (Fig. 6e) [38] because Sb was removed during the thin-film growth process and was not completely incorporated into the thin film (Section 3.1).

■ Ag thin film

(a) Eluted Ag

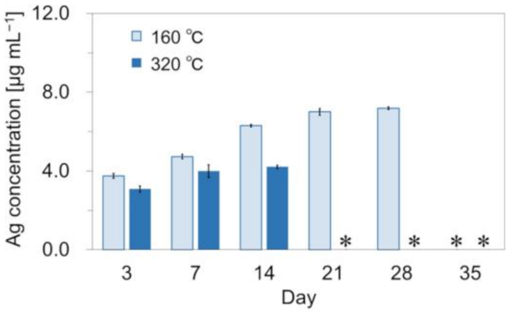

■ Bi-doped Ag thin film

(b) Eluted Ag

(c) Eluted Bi

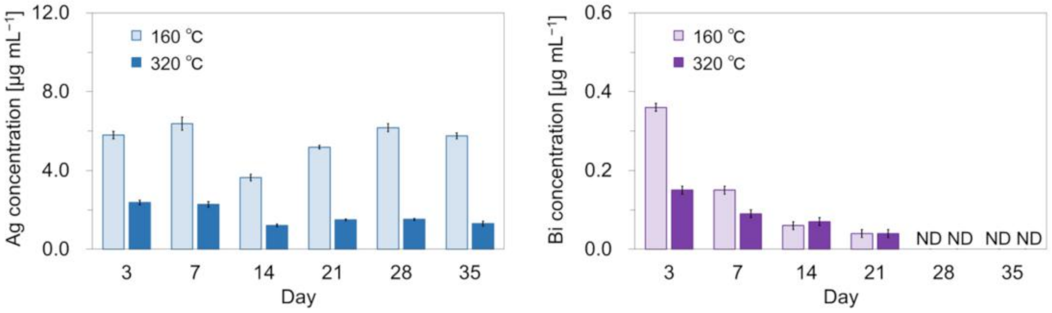

■ Sb-doped Ag thin film

(d) Eluted Ag

(e) Eluted Sb

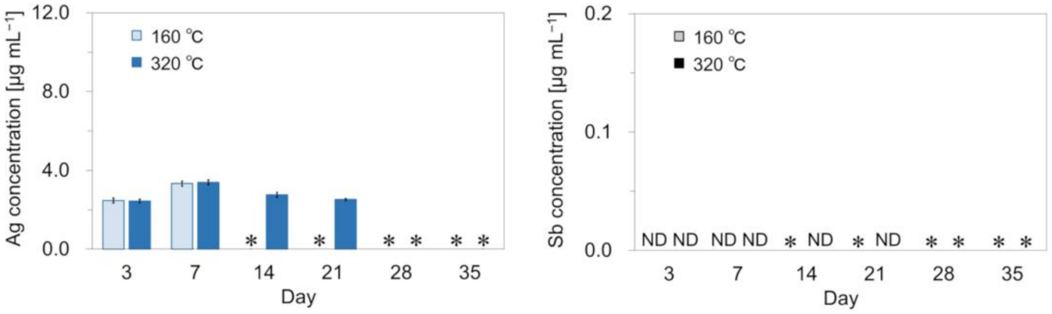

Fig. 6. Elution of Ag, Bi, and Sb in pH 9 buffer from thin films of (a) Ag, (b, c) Bi-doped Ag, and (d, e) Sb-doped Ag at growth temperatures of 160 and 320 °C. The asterisks (*) indicate that the thin film had detached from the PI film. Data are expressed as the average ± standard deviation.

The elution tendencies of Bi and Sb were in good agreement with the XRF measurements and the behavior of Bi and Sb during the sputtering growth of Ag thin films as described in Section 3.1.

As discussed in Section 3.4.2, the tensile strain in the Ag thin films was decreased by Bi or Sb doping, with a small $|SFP|$ value indicating low thin-film strain. These changes in thin-film strain may enhance the adhesiveness as mentioned in Section 1 [20, 21]. The period until detachment of the grown thin film from the PI film was strongly correlated to the $|SFP|$ values plotted in Fig. 4, where smaller $|SFP|$ values caused by the decrease in tensile strain were associated with a longer time for film detachment. Specifically, the undoped Ag thin films displayed a lower $|SFP|$ value at a growth temperature of 160 °C, while the Sb-doped Ag thin films exhibited a lower $|SFP|$ value at a growth temperature of 320 °C. The Bi-doped Ag thin films showed low $|SFP|$ values at both growth temperatures.

The thin-film strain was suppressed by Bi doping at growth temperatures of both 160 and 320 °C and by Sb doping at a growth temperature of 320 °C. Under these growth conditions, these dopants decreased tensile strain in the thin films and improved the adhesiveness between the thin films and PI films. In contrast, non-uniform growth (Fig. 1c) led to increased $|SFP|$ in the Sb-doped Ag thin film grown at 160 °C. The interfacial strength between the Sb-doped Ag thin film and PI film was considered to be decreased by the poorer crystallinity due to non-uniform growth [39]. This is inferred to be the reason why the Sb-doped Ag film grown at 160 °C detached from the PI film earlier than the one grown at 320 °C.

4. Conclusion

In this study, we investigated the effects of Bi and Sb doping on the stability of Ag thin films grown on PI films. Bi assisted the [111] growth of Ag thin films at the growth temperature of 160 °C, while the formation of Bi clusters suppressed the [111] growth of Ag thin films at the growth temperature of 320 °C. Although Sb doping led to non-uniform growth of the Ag thin films at the growth temperature of 160 °C, it assisted the [111] growth of the Ag thin films at the growth temperature of 320 °C. The thin-film strain, which affects the adhesiveness between the grown thin films and PI substrates, was estimated by XRD analysis. The results revealed that the strain present in the PI film was not applied to the deposited Ag thin films. Doping with Bi or Sb reduced the strain of the Ag thin films and prevented their detachment from the PI film in pH 9 buffer, except for the Sb-doped Ag thin film grown at 160 °C. These results of this study demonstrate that Bi and Sb doping assists the growth of Ag thin films and enhances their stability by improving both the (111) orientation and the adhesiveness between the Ag thin film and PI substrate. We believe that these findings will prove useful for improving the reliability of devices based on Ag thin films.

Limitations

This study has some limitations. First, the long-term stability of the films was not evaluated under different environmental conditions (e.g., humidity, temperature fluctuations). Second, the thin films were not grown under various dopant levels and growth temperatures. Third, the obtained results did not expand on the relationship with other factors (e.g., surface roughness and grain boundaries). Therefore, further confirmation of these results is necessary before applying Bi- and Sb-doped Ag thin films in various products.

Acknowledgements

This work was supported by Japan Society for the Promotion of Science (JSPS) a Grant-in-Aid for Scientific Research (B) (grant number 23K21524) to Junko Fujihara.

Author contributions

Conceptualization: Naoki Nishimoto; Investigation and data curation: Naoki Nishimoto, Junko Fujihara; Formal analysis: Naoki Nishimoto; Funding acquisition: Junko Fujihara; Writing – original draft preparation: Naoki Nishimoto; Writing – review and editing: Naoki Nishimoto, Junko Fujihara

Funding

This work was supported by grant number 23K21524. Junko Fujihara has received research support from Japan Society for the Promotion of Science.

Data availability

Not applicable.

Declarations

Conflict of interest

The authors declare that they have no conflict of interest.

References

[1] N. Manjula, S. Pulikkutty, T.-W. Chen, S.-M. Chen, C.H. Fan, M.A. Ali, F.M. Al-Hemaid, Electrochemical sensor based on cerium niobium oxide nanoparticles modified electrode for sensing of environmental toxicity in water sample, Colloids Surf. A: Physicochem. Eng. Asp. 637, 128277 (2022). https://doi.org/10.1016/j.colsurfa.2022.128277

[2] T. Prohaska, J. Irrgeher, J. Benefield, J.K. Böhlke, L.A. Chesson, T.B. Coplen, T. Ding, P.J.H. Dunn, M. Gröning, et al., Standard atomic weights of the elements 2021 (IUPAC Technical Report), Pure Appl. Chem 94, 573–600 (2022). https://doi.org/10.1515.pac-2019-0603

[3] T.D. Aslam, M.A. McBride, N. Rai, D.E. Hooks, J.A. Stull, B.J. Jensen, Modeling atomically mixed graded density impactors, J. Appl. Phys. 131, 225901 (2022). https://doi.org/10.1063/5.0085223.

[4] A. Liu, X. Ren, C. Wang, J. Zhang, C. Du, R. Han, M. An, DMH and NA-based cyanide-free silver electroplating bath: a promising alternative to cyanide ones in microelectonics, Ionics 27, 417–422 (2021). https://doi.org/10.1007/s11581-020-03541-

[5] Q. Wang, Y. Zhang, Q. Li, L. Chen, H. Liu, M. Ding, H. Dong, Y. Mou, Therapeutic applications of antimicrobial silver-based biomaterials in density, Int. J. Nanomedicine 17, 443–462 (2022). https://doi.org/10.2147/IJN.S349238

[6] Y.-T. Cheng, K.-L. Lin, C.-C. Lin, Preparing Silver-Copper pastes in accordance with percolation theory for die attach bonding, Mater. Chem. Phys. 297, 127391 (2023). https://doi.org/10.1016/j.matchemphys.2023.127391

[7] A.C. Phillips, D.M. Fryauf, N. Kobayashi, M.J. Bolte, B. Dupraw, C. Ratliff, T.

Pfister, D. Cowley, Progress and new techniques for protected-silver coatings, Advances in Optical and Mechanical Technologies for Telescopes and Instrumentation, 9151, 436–445 (2014). https://doi.org/10.1117/12.2055706

[8] B. Zheng, Q. Zhu, Y. Zhao, Fabrication of high-quality silver nanowire conductive film and its application for transparent film heaters, J. Mater. Sci. Technol. 71, 221–227 (2021). https://doi.org/10.1016/j.jmst.2020.07.021

[9] C.J. Heard, R.L. Johnston, J.C. Schön, Energy landscape exploration of sub-nanometer copper-silver clusters, ChemPhysChem 16, 1461–1469 (2015). https://doi.org/10.1002/cphc.201402887

[10] R. Tran, Z. Xu, B. Radhakrishnan, D. Winston, W. Sun, K.A. Persson, S.P. Ong, Surface energy of elemental crystals, Sci. Data 3, 160080 (2016). https://doi.org/10.1038/sdata.2016.80

[11] J.W. Elmer, T.A. Palmer, E.D. Specht, Direction observations of rapid diffusion of Cu in Au thin films using in-situ x-ray diffraction, J. Vac. Sci. Technol. A 24, 978–987 (2006). https://doi.org/10.1116/1.2204926

[12] K.Y. Chan, B.S. Tao, Effect of Ar pressure on grain size of magnetron sputter-deposited Cu thin films, IET Sci. Meas. Technol. 1, 87–90 (2007). https://doi.org/10.1049/iet-smt:20060110

[13] H. Khachatryan, S.-N. Lee, K.-B. Kim, H.-K. Kim, M. Kim, Al thin films: The effect of substrate type on Al film formation and morphology, J. Phys. Chem. Solids 122, 109–117 (2018). https://doi.org/10.1016/j.jpcs.2018.06.018

[14] N. Nishimoto, J. Fujihara, Improvement of the structural properties and environmental stability of flexible InSb thin films by dopant-assisted crystallization, Appl. Phys. A 128, 550 (2022). https://doi.org/10.1007/s00339-022-05694-8

[15] N. Nishimoto, J. Fujihara, Bismuth-assisted low-temperature growth of flexible GaSb thin films by multi-cathode RF magnetron sputtering, J. Mater. Sci. 58, 11174–11186 (2023). https://doi.org/10.1007/s10853-023-08735-6

[16] T. Cui, R. Lv, Z.-H. Huang, F. Kang, K. Wang, D. Wu, Effect of sulfur on enhancing nitrogen-doping and magnetic properties of carbon nanotubes, Nanoscale Res. Lett. 6, 77 (2011). https://doi.org/10.1186/1156-276X-6-77

[17] C. Cai, L. Zhai, C. Zou, Z. Li, L. Zhang, Y. Yang, S. Huang, $Cu_{1.94}S$-assisted growth of wurzite $CuInS_2$ nanoleaves by in situ copper sulfidation, Nanoscale Res. Lett. 10, 294 (2015). https://doi.org/10.1186/s11671-015-0996-y

[18] M.S. Seifner, P. Pertl, J. Bernardi, S. Biswas, J.D. Holmes, S. Barth, Lead-supported germanium nanowire growth, Mater. Lett. 173, 248–251 (2016). https://doi.org/10.1016/j.matlet.2016.03.066

[19] A. Ajay, H. Jeong, T. Schreitmüller, M. Döblinger, D. Ruhstorfer, N. Mukhundhan, P.A.L.M. Koolen, J.J. Finley, G. Koblmüller, Enhanced growth and properties of non-catalytic GaAs nanowires via Sb surfactant effects, Appl. Phys. Lett. 121, 072107 (2022). https://doi.org/10.1063/5.0095952

[20] Y.-C. Huang, S.-Y. Chang, C.-H. Chang, Effect of residual stresses on mechanical properties and interface adhesion strength of SiN thin films, Thin Solid Films 517, 4857–4861 (2009).

[21] A. Moridi, H. Ruan, L.C. Zhang, M. Liu, Residual stresses in thin film systems: Effects of lattice mismatch, thermal mismatch and interface dislocations, Int. J. Solids Struct. 50, 3562–3569 (2013). http://dx.doi.org/10.1016/j.ijsolstr.2013.06.022

[22] F. Shakerian, A.M. Haji Shabani, S. Dadfarnia, M. Kazemi Avanji, Hydride generation atomic absorption spectrometric determination of bismuth after separation

and preconcentration with modified alumina, J. Sep. Sci. 38, 677–682 (2015). https://doi.org/10.1002/jssc.201401050

[23] K. Kargosha, A. Valadkhani, Preconcentration and direct determination of As and Bi in aqueous and solid samples using hydride generation atomic fluorescence, Atom. Spectrosc. 38, 194–199 (2017). https://doi.org/10.46770/AS.2017.06.004

[24] J. Fujihara, N. Nishimoto, Total antimony analysis by hydride generation-microwave plasma-atomic emission spectroscopy with applications, Microchem. J. 157, 104992 (2020). https://doi.org/10.1016/j.microc.2020.104992

[25] R. Cao, X. Yang, J. Terry, P. Pianetta, Microscopic study of the surfactant-assisted Si, Ge epitaxial growth, Appl. Phys. Lett. 61, 2347–2349 (1992). https://doi.org/10.1063/1.108239

[26] T.P. Menasuta, K.A. Grossklaus, J.H. McElearney, T.E. Vandervelde, Bismuth surfactant enhancement of surface morphology and film quality of MBE-grown GaSb (100) thin films over a wide range of growth temperatures, J. Vac. Sci. Technol. A 42, 032703 (2024). https://doi.org/10.1116/6.0003458

[27] H.F. Winters, H.J. Coufal, W. Eckstein, Influence of energy reflected from the target on thin film characteristics, J. Vac. Sci. Technol. A 11, 657–663 (1993). https://doi.org/10.1116/1.578787

[28] N. Yamada, S. Suzuki, K. Suzuki, A. Tanaka, R. Morita, C. Che, G. Frohberg, Investigation of the Influence of Different Solute on Impurity Diffusion in Liquid Sn using the Shear Cell Technique, Int. J. Microgravity Sci. Appl. 35, 350402 (2018). https://doi.org/10.15011//jasma.35.350402

[29] D. Kandel, E. Kaxiras, The surfactant effect in semiconductor thin film growth, Solid State Physics 54, 219–262 (2000). https://doi.org/10.1016/S0081-1947(08)60249-

0

[30] R.P.I Adler, H.M. Otte, C.N.J. Wagner, Determination of dislocation density and stacking fault probability from X-ray powder pattern peak profiles, Metall. Trans. 1, 2375–2382 (1970). https://doi.org/10.1007/BF03038366

[31] E. Anastassakis, Elastic distortions of strained layers grown epitaxially in arbitrary directions, J. Cryst. Growth 114, 647–655 (1991). https://doi.org/10.1016/0022-0248(91)90411-W

[32] D. Zhang, Y.-C. Wu, M. Yang, X. Liu, C.Ó. Coileáin, H. Xu, M. Abid, M. Abid, J.-J. Wang, et al., Probing thermal expansion coefficients of monolayers using surface enhanced Raman scattering, RSC Adv. 6, 99053–99059 (2016). https://doi.org/10.1039/c6ra20623a

[33] K.-E. Kim, M.H. Jee, D.H. Baik, Effect of Terephthaloyl Chloride Comonomer on Thermal and Optical Properties of Colorless and Transparent Polyimide Films Based on 4, 4′-(Hexafluoroisopropylidene) Diphthalic Anhydride and Bis(3-aminophenyl) Sulfone, Fiber. Polym. 24, 2275–2282 (2023). https://doi.org/10.1007/s12221-023-00211-x

[34] R.E. Schramm, R.P. Reed, Stacking fault energies of fcc Fe-Ni alloys by X-ray diffraction line profile analysis, Metall. Trans. A 7, 359–363 (1976). https://doi.org/10.1007/BF02642831

[35] M. Walter, L.M. Roncery, S. Weber, L. Leich, W. Theisen, XRD measurement of stacking fault energy of Cr-Ni austenitic steels: influence of temperature and alloying elements, J. Mater. Sci. 55, 13424–13437 (2020). https://doi.org/10.1007/s10853-020-04953-4

[36] B. Neding, O.I. Gorbatov, J.-C. Tseng, P. Hedström, In situ bulk observations and

ab initio calculations revealing the temperature dependence of stacking fault energy in Fe-Cr-Ni alloys, Metallurgical and Materials Transactions A 52, 5357–5366 (2021). https://doi.org/10.1007/s11661-021-06473-5

[37] L. Zhang, C. Lu, K. Tieu, G. Michal, J. Zhang and G. Deng, Tension/compression asymmetry of grain boundaries with non-planar structure, Mater. Res. Express 3, 085025 (2016). https://doi.org/10.1088/2053-1591/3/8/085025

[38] C.J. Boreiko, T.G. Rossman, Antimony and its compounds: Health impacts related to pulmonary toxicity, cancer, and genotoxicity, Toxicol. Appl. Pharmacol. 403, 115156 (2020). https://doi.org/10.1016/j.taap.2020.115156

[39] S.N. Basu, H. Wu, V. Gupta, V. Kireev, The effect of structure and chemistry on the strength of FeCrAl(Y)/sapphire interfaces: II. Strength of interfaces, Mater. Sci. Eng. A 349, 265–271 (2003). https://doi.org/10.1016/S0921-5093(02)00791-8

Table 1. Thicknesses of Ag, Bi-doped Ag, and Sb-doped Ag thin films grown at 160 °C and 320 °C.

Growth temperature [°C]	Film thickness [nm]		
	Ag thin film	Bi-doped Ag thin film	Sb-doped Ag thin film
160	369	349	368
320	380	363	394